Article

Intrinsic Dynamic and Static Nature of Halogen Bonding in Neutral Polybromine Clusters, with the Structural Feature Elucidated by QTAIM Dual-Functional Analysis and MO Calculations

Satoko Hayashi *, Taro Nishide, Eiichiro Tanaka and Waro Nakanishi *

Faculty of Systems Engineering, Wakayama University, 930 Sakaedani, Wakayama 640-8510, Japan; s209004@wakayama-u.ac.jp (T.N.); s216156@wakayama-u.ac.jp (E.T.)
* Correspondence: hayashi3@sys.wakayama-u.ac.jp (S.H.); nakanisi@sys.wakayama-u.ac.jp (W.N.); Tel.: +81-73-457-8252 (S.H. & W.N.)

Abstract: The intrinsic dynamic and static nature of noncovalent Br-∗-Br interactions in neutral polybromine clusters is elucidated for Br_4–Br_{12}, applying QTAIM dual-functional analysis (QTAIM-DFA). The asterisk (∗) emphasizes the existence of the bond critical point (BCP) on the interaction in question. Data from the fully optimized structures correspond to the static nature of the interactions. The intrinsic dynamic nature originates from those of the perturbed structures generated using the coordinates derived from the compliance constants for the interactions and the fully optimized structures. The noncovalent Br-∗-Br interactions in the L-shaped clusters of the C_s symmetry are predicted to have the typical hydrogen bond nature without covalency, although the first ones in the sequences have the vdW nature. The L-shaped clusters are stabilized by the $n(Br) \rightarrow \sigma^*(Br–Br)$ interactions. The compliance constants for the corresponding noncovalent interactions are strongly correlated to the $E(2)$ values based on NBO. Indeed, the MO energies seem not to contribute to stabilizing Br_4 (C_{2h}) and Br_4 (D_{2d}), but the core potentials stabilize them, relative to the case of $2Br_2$; this is possibly due to the reduced nuclear–electron distances, on average, for the dimers.

Keywords: ab initio calculations; quantum theory of atoms-in-molecules (QTAIM); bromide; structures

1. Introduction

Halogen bonding is of current and continuous interest [1,2]. A lot of information relevant to halogen bonding has been accumulated so far [3]. Halogen bonding has been discussed on the basis of the shorter distances between halogen and other atoms in crystals [4–6]. The short halogen contacts are found in two types: symmetric (type **I**) and bent (type **II**) geometries. The bonding has also been investigated in the liquid [7,8] and gas [9] phases. The nature of halogen bonding has been discussed based on the theoretical background on the molecular orbital description for the bonding and the σ-hole developed on the halogen atoms, together with the stability of the structural aspects [10]. We also reported the dynamic and static nature of Y–X—$\pi(C_6H_6)$ interactions recently [11]. Halogen bonding is applied to a wide variety of fields in chemical and biological sciences, such as crystal engineering, supramolecular soft matters, and nanoparticles. Efforts have been made to unify and categorize the accumulated results and establish the concept of halogen bonding [3,12–15].

Structures of halogen molecules (X_2) have been reported, as determined by X-ray crystallographic analysis for X = Cl, Br, and I [16–18]. The behavior of bromine–bromine interactions has been reported for the optimized structures of Br_2–Br_5 in the neutral and/or charged forms, together with Br_1, so far [19,20]. Figure 1 draws the observed structure of Br_2, for example. The bromine molecules seem to exist as a zig-zag structure in the infinite chains in crystals. One would find the linear alignment of three Br atoms in an

L-shaped dimer ((Br_2)$_2$; Br_4) and the linear alignment of four Br atoms in a double L-shaped trimer ((Br_2)$_3$; Br_6) in a planar Br_2 layer in addition to Br_2 itself. The linear four Br atoms are located in the two L-shaped dimers of Br_6, overlapped at the central Br_2. While the L-shaped dimers seem to construct the zig-zag type infinite chains, the linear four Br atoms construct linear infinite chains. The attractive $n_p(Br) \rightarrow \sigma^*(Br–Br)$ $\sigma(3c–4e)$ (three center–four electron interaction of the σ-type) and $n_p(Br) \rightarrow \sigma^*(Br–Br) \leftarrow n_p(Br)$ $\sigma(4c–6e)$ must play a very important role to stabilize Br_4 and Br_6, respectively, where $n_p(Br)$ stands for the p-type nonbonding orbital of Br in the plane, perpendicular to the molecular Br_2 axis, and $\sigma^*(Br–Br)$ is the σ^*-orbital of Br_2. The crystal structures of Cl_2 and I_2 are very similar to that of Br_2.
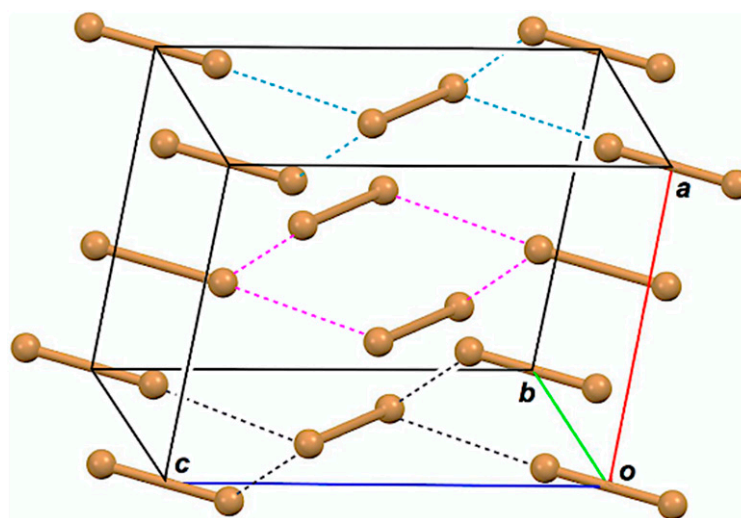

Figure 1. Structure of Br_2, determined by X-ray crystallographic analysis [17].

We have been very interested in the behavior of halogen bonding in polyhalogen clusters, together with the structures. How can the interactions in the polyhalogen clusters be clarified? We propose QTAIM dual-functional analysis (QTAIM-DFA) [21–25] based on the quantum theory of atoms in molecules (QTAIM) approach introduced by Bader [26,27] to classify and characterize the various interactions effectively [28]. In QTAIM-DFA, $H_b(r_c)$ are plotted versus $H_b(r_c) - V_b(r_c)/2$ ($= (\hbar^2/8m)\nabla^2\rho_b(r_c)$ (see Equation (SA2) in the supplementary materials), where $\rho_b(r_c)$, $H_b(r_c)$, and $V_b(r_c)$ stand for the charge densities, total electron energy densities, and potential energy densities, respectively, at bond critical points (BCPs, $*$) on the bond paths (BPs) in this paper [26]. The kinetic energy densities at BCPs will be similarly denoted by $G_b(r_c)$ [26]. A chemical bond or an interaction between Br and Br is denoted by Br-$*$-Br in this work, where the asterisk emphasizes the existence of a BCP on a BP for Br–Br [26,27]. In our treatment, data from the fully optimized structures are plotted together with those from the perturbed structures around the fully optimized ones. The static nature of the interactions corresponds to the data from the fully optimized structures, which are analyzed using polar coordinate (R, θ) representation [21–25]. On the other hand, the dynamic nature originates based on the data from both the perturbed and fully optimized structures [21–25]. The plot is expressed by (θ_p, κ_p), where θ_p corresponds to the tangent line and κ_p is the curvature of the plot. θ and θ_p are measured from the *y*-axis and the *y*-direction, respectively. We call (R, θ) and (θ_p, κ_p) the QTAIM-DFA parameters [29].

Interactions are classified by the signs of $\nabla^2\rho_b(r_c)$ and $H_b(r_c)$, based on the QTAIM approach. The interactions are called shard shell (SS) interactions when $\nabla^2\rho_b(r_c) < 0$ and closed-shell (CS) interactions when $\nabla^2\rho_b(r_c) > 0$ [26]. In particular, CS interactions are called *pure* CS (*p*-CS) interactions when $H_b(r_c) > 0$ and $\nabla^2\rho_b(r_c) > 0$. We call interactions where $H_b(r_c) < 0$ and $\nabla^2\rho_b(r_c) > 0$ *regular* CS (*r*-CS) interactions, which clearly distinguishes

these interactions from the p-CS interactions. The signs of $\nabla^2\rho_b(\mathbf{r}_c)$ can be replaced by those of $H_b(\mathbf{r}_c) - V_b(\mathbf{r}_c)/2$ because $(\hbar^2/8m)\nabla^2\rho_b(\mathbf{r}_c) = H_b(\mathbf{r}_c) - V_b(\mathbf{r}_c)/2$ (see Equation (SA2) in the supporting information). Indeed, $H_b(\mathbf{r}_c) - V_b(\mathbf{r}_c)/2 = 0$ corresponds to the borderline between the classic covalent bonds of SS and the noncovalent interactions of CS, but $H_b(\mathbf{r}_c) = 0$ appears to be buried in the noncovalent interactions of CS. As a result, it is difficult to characterize the various CS interactions based on the signs of $H_b(\mathbf{r}_c) - V_b(\mathbf{r}_c)/2$ and/or $H_b(\mathbf{r}_c)$. In QTAIM-DFA, the signs of the first derivatives of $H_b(\mathbf{r}_c) - V_b(\mathbf{r}_c)/2$ and $H_b(\mathbf{r}_c)$ $(\mathrm{d}(H_b(\mathbf{r}_c) - V_b(\mathbf{r}_c)/2)/\mathrm{d}r$ and $\mathrm{d}H_b(\mathbf{r}_c)/\mathrm{d}r$, respectively, where r is the interaction distance) are used to characterize CS interactions, in addition to those of $H_b(\mathbf{r}_c) - V_b(\mathbf{r}_c)/2$ and $H_b(\mathbf{r}_c)$, after analysis of the plot. While the former corresponds to (θ_p, κ_p), the latter does to (R, θ). The analysis of the plots enables us to characterize the various CS interactions more effectively. Again, the details are explained later.

The perturbed structures necessary for QTAIM-DFA can be generated. Among them, a method employing the coordinates corresponding to the compliance constants C_{ii} for internal vibrations is shown to be highly reliable to generate the perturbed structures [30–39]. The method, which we proposed recently, is called CIV. The dynamic nature of interactions based on the perturbed structures with CIV is described as the "intrinsic dynamic nature of interactions" since the coordinates are invariant to the choice of coordinate system. Rough criteria that distinguish the interaction in question from others are obtained by applying QTAIM-DFA with CIV to standard interactions. QTAIM-DFA and the criteria are explained in the appendix of the supplementary materials using Schemes SA1–SA3, Figures SA1 and SA2, Table SA1, and Equations (SA1)–(SA7). The basic concept of the QTAIM approach is also explained.

QTAIM-DFA, using the perturbed structures generated with CIV, is well-suited to elucidate the intrinsic dynamic and static nature of halogen–halogen interactions in the polyhalogen clusters. As the first step to clarify the nature of various types of halogen–halogen interactions in the polyhalogen clusters, the nature of each bromine–bromine interaction in the neutral polybromine clusters is elucidated by applying QTAIM-DFA. Various types of structures and interactions are found in the optimized structures of polybromine clusters, other than those observed in the crystals. Here, we present the results of investigations on the polybromine clusters, together with the structural feature, elucidated with QTAIM-DFA and QC calculations.

2. Methodological Details in Calculations

The structures were optimized by employing Gaussian 09 programs [40]. The 6-311+G(3df) basis [41–44] set was applied to optimize the structures of neutral polybromine clusters, Br_2–Br_{12}. The Møller–Plesset second-order energy correlation (MP2) level [45–47] was applied for the optimizations. Optimized structures were confirmed by frequency analysis. The results of the frequency analyses were employed to calculate the C_{ij} values and coordinates corresponding to C_{ii} [30,34–36]. The $\rho_b(\mathbf{r}_c)$, $H_b(\mathbf{r}_c) - V_b(\mathbf{r}_c)/2$ $(=(\hbar^2/8m)\nabla^2\rho_b(\mathbf{r}_c))$, and $H_b(\mathbf{r}_c)$ values were calculated using the Gaussian 09 program package [40], with the same method applied to the optimizations. Data were analyzed with the AIM2000 [48,49] and AIMAll [50] programs.

Coordinates corresponding to the compliance constants for an internal coordinate i of the internal vibrations ($\mathbf{C}_i$) were employed to generate the perturbed structures necessary in QTAIM-DFA [21–25]. Equation (1) explains the method to generate the perturbed structures with CIV. An i-th perturbed structure in question ($\mathbf{S}_{iw}$) was generated by the addition of the coordinates ($\mathbf{C}_i$) corresponding to C_{ii} to the standard orientation of a fully optimized structure ($\mathbf{S}_o$) in the matrix representation. The coefficient g_{iw} in Equation (1) controls the difference in structures between $\mathbf{S}_{iw}$ and $\mathbf{S}_o$: g_{iw} are determined to satisfy Equation (2) for the interaction in question, where r and r_o show the distances in question in the perturbed and fully optimized structures, respectively, with a_o of Bohr radius (0.52918 Å) [21–25,30].

$$\mathbf{S}_{iw} = \mathbf{S}_o + g_{iw} \times \mathbf{C}_i \tag{1}$$

$$r = r_o + wa_o \quad (w = (0), \pm 0.05 \text{ and } \pm 0.1; a_o = 0.52918 \text{ Å}) \tag{2}$$

$$y = c_o + c_1 x + c_2 x^2 + c_3 x^3 \quad (R_c^2: \text{square of correlation coefficient}) \tag{3}$$

In the QTAIM-DFA treatment, $H_b(r_c)$ are plotted versus $H_b(r_c) - V_b(r_c)/2$ for the data of five points of $w = 0$, ± 0.05, and ± 0.1 in Equation (2). Each plot is analyzed using a regression curve of the cubic function, as shown in Equation (3), where $(x, y) = (H_b(r_c) - V_b(r_c)/2, H_b(r_c))$ (R_c^2 (square of correlation coefficient) > 0.99999 in the norm) [25].

3. Results and Discussion

3.1. Structural Optimizations of Polybromine Clusters, Br_6–Br_{12}

Structures of the neutral Br_2–Br_{12} clusters were optimized with MP2/6-311+G(3df). The structural parameters for the optimized structures of minima for Br_2–Br_6 and Br_8–Br_{12} are collected in Tables S1 and S2, respectively. Some transition states (TSs) for Br_4 and Br_6 were also calclaterd. The notation of C_s-L_m (m = 1–5) is used for the linear L-shaped clusters of the C_s symmetry, where m stands for the number of noncovalent interactions in Br_{2m+2} (m = 1–5). Cyclic structures are also optimized, retaining the higher symmetries. The optimized structures are not shown in figures, but they can be found in the molecular graphs with the contour maps of $\rho(r)$ for the linear-type bromine clusters Br_4–Br_{12} (C_s-L_m (m = 1–5)) and for the cyclic bromine clusters Br_4–Br_{12}, drawn on the optimized structures with MP2/6-311+G(3df) [51]. The energies for the formation of Br_4–Br_6 and Br_8–Br_{12} are given in Tables S1 and S2, respectively, from the components ($\Delta E = E(Br_{2k}) - kE(Br_2)$) on the energy surfaces (ΔE_{ES}) and those with the collections of zero-point energies (ΔE_{ZP}). The ΔE_{ZP} values were plotted versus ΔE_{ES}. The plot is shown in Figure S1, which gives an excellent correlation ($y = 0.940x + 0.129$; R_c^2 (square of correlation coefficient) = 0.9999) [52]. Therefore, the ΔE_{ES} values are employed for the discussion.

The behavior of the neutral dibromine clusters (Br_4) is discussed first. Three structures were optimized for Br_4 as minima with some TSs. The minima are the L-shaped structure of C_s symmetry (Br_4 (C_s-L_1)) [19], the cyclic structure of C_{2h} symmetry (Br_4 (C_{2h})), and the tetrahedral type of D_{2d} symmetry (Br_4 (D_{2d})). A TS of the C_s symmetry was detected between Br_4 (C_s-L_1) and Br_4 (C_{2h}), and two TSs of the C_1 symmetry were between Br_4 (C_{2h}) and Br_4 (D_{2d}) and between Br_4 (D_{2d}) and Br_4 (C_s-L_1). They are called TS (C_s: C_s, C_{2h}), TS (C_1: C_{2h}, D_{2d}), and TS (C_1: D_{2d}, C_s), respectively. The three minima will be converted to each other through the three TSs. A TS between Br_4 (C_s-L_1) and its topological isomer was also detected, which is called TS (C_{2v}: C_s, C_s); however, further effort was not made to search for similar TSs between Br_4 (C_{2h}) and its topological isomer and between Br_4 (C_{2d}) and its topological isomer.

Figure 2 draws the energy profiles for the optimized structures of minima, Br_4 (C_s-L_1), Br_4 (C_{2h}), and Br_4 (D_{2d}), together with the TSs TS (C_s: C_s, C_{2h}), TS (C_s: C_{2h}, D_{2d}), TS (C_1: C_{2d}, C_s), and TS (C_{2v}: C_s, C_s). The optimized structures are not shown in the figures, but they can be found in the molecular graphs shown in Figure 2, illustrated on the optimized structures. All BCPs expected are detected clearly, together with RCPs and a CCP [26]. The ΔE_{ES} value of -10.7 kJ mol^{-1} for the formation of Br_4 (C_s-L_1) seems very close to the border area between the vdW and typical hydrogen bond (*t*-HB) adducts. The driving force for the formation of Br_4 (C_s-L_1) must be Br_3 σ(3c–4e) of the $n_p(Br) \to \sigma^*(Br–Br)$ type. The interactions in Br_4 (C_{2h}) and Br_4 (D_{2d}) seem very different from those in Br_4 (C_s-L_1). The ΔE_{ES} values of Br_4 (C_{2h}) (-8.0 kJ mol^{-1}) and Br_4 (D_{2d}) (-9.1 kJ mol^{-1}) are close to that for Br_4 (C_s-L_1) (-10.7 kJ mol^{-1}). Moreover, the values for TS (C_s: C_s, C_{2h}) (-7.4 kJ mol^{-1}), TS (C_1: C_{2h}, D_{2d}) (-7.6 kJ mol^{-1}), TS (C_1: D_{2d}, C_s) (-7.0 kJ mol^{-1}), and TS (C_{2v}: C_s, C_s) (-8.7 kJ mol^{-1}) are not so different from those for the minima.
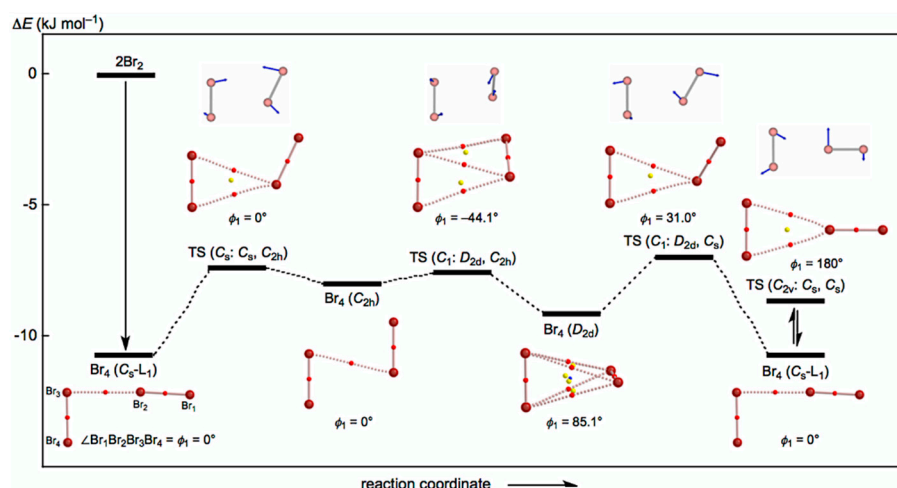
Figure 2. Energy profile with molecular graphs for the structures of Br_4 clusters, optimized with MP2/6-311+G(3df).

In the case of Br_6, three structures of the linear C_s symmetry (Br_6 (C_s-L_2)), the linear C_2 symmetry (Br_6 (C_2)), and the cyclic C_{3h} symmetry (Br_6 (C_{3h}-c)) were optimized typically as minima. The linear Br_6 clusters of C_{2h} symmetry (Br_6 (C_{2h})) and C_{2v} symmetry (Br_6 (C_{2v})), similar to Br_6 (C_2), were also optimized, of which the torsional angles, $\phi(^1Br^2Br^5Br^6Br)$ ($=\phi_3$), were $0°$ and $180°$, respectively. One imaginary frequency was detected for each; therefore, they are assigned to TSs between Br_6 (C_2) and the topological isomer on the different reaction coordinates. Further effort was not made to search for TSs.

The ΔE_{ES} value for Br_6 (C_s-L_2) was predicted to be -22.6 kJ mol^{-1}. The magnitude is slightly larger than the double value for Br_4 (C_s-L_1) ($\Delta E_{ES} = -10.7$ kJ mol^{-1}). Two types of σ (3c–4e) operate to stabilize Br_6 (C_s-L_2). One, σ(3c–4e), seems similar to that in Br_4 (C_s-L_1), but the other would be somewhat different. Namely, the second interaction would contribute to ΔE_{ES} somewhat more than that of the first one in the formation of Br_6 (C_s-L_2). On the other hand, the linear interaction in Br_6 (C_2) can be explained by σ(4c–6e) of the $n_p(Br) \rightarrow \sigma^*(Br–Br) \leftarrow n_p(Br)$ type. The magnitude of ΔE_{ES} of Br_6 (C_2) seems slightly smaller than that of Br_6 (C_s-L_2) but is very close to the double value for Br_4 (C_s-L_1). The magnitude of ΔE_{ES} for Br_6 (C_{3h}-c) is close to the triple value of Br_4 (C_s-L_1). One finds triply degenerated σ(3c–4e) interactions in Br_6 (C_{3h}-c). The similarity in the interactions for Br_4 (C_s-L_1), Br_6 (C_2), and Br_6 (C_{3h}-c) will be discussed again later. The magnitudes of ΔE_{ES} become proportionally larger to the size of the clusters, as shown in Figures S1 and S2. The ΔE_{ES} values are plotted versus k in Br_{2k} ($2 \leq k \leq 6$) for the C_s-L_m type. The results are shown in Figure S2. Contributions from inner σ(3c–4e) (named r_{in}) to ΔE_{ES} seem slightly larger than those from σ(3c–4e) in the front end and end positions (named r_2 and r_ω, respectively).

After examination of the optimized structures, the next extension is to clarify the nature of Br-∗-Br interactions by applying QTAIM-DFA. The contour plots are discussed next.

3.2. Molecular Graphs with Contour Plots of Polybromine Clusters

Figure 3 illustrates the molecular graphs with contour maps of $\rho(r)$ for the linear type of Br_4 (C_s-L_1)–Br_{12} (C_s-L_5), drawn on the structures optimized with MP2/6-311+G(3df). Figure 4 draws the molecular graphs with contour maps of $\rho(r)$ for Br_4–Br_{12}, other than those for Br_4 (C_s-L_1)–Br_{12} (C_s-L_5), calculated with MP2/6-311+G(3df) [53,54] (see also Figure S3). All BCPs expected are detected clearly, together with RCPs and a CCP containing those for noncovalent Br-∗-Br interactions, which are located at the (three-dimensional) saddle points of $\rho(r)$.
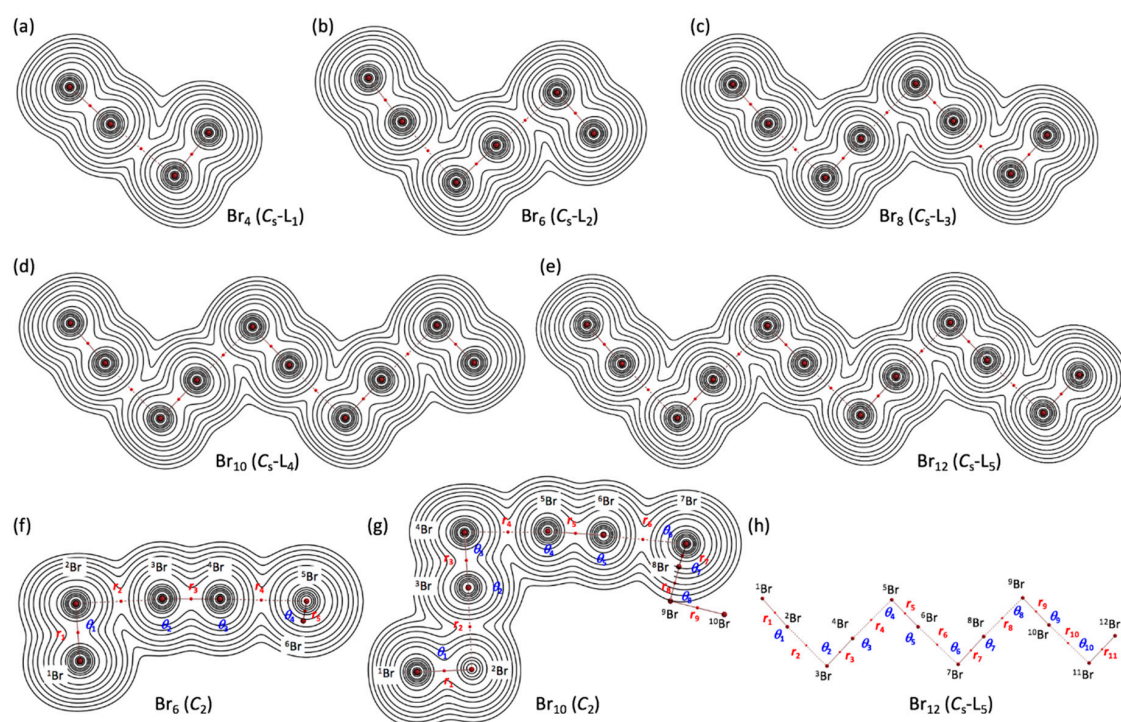
Figure 3. Molecular graphs with contour plots of $\rho(r)$ for the linear-type bromine clusters of Br_4–Br_{12}, calculated with MP2/6-311+G(3df). (**a**–**e**) for the linear C_s-L_m type, (**f**,**g**) for the C_2 type, and (**h**) for the notations of atoms, bonds, and angles, exemplified by B_{12} (C_s-L_5). BCPs are denoted by red dots, and BPs (bond paths) are by pink lines. Bromine atoms are in reddish-brown.
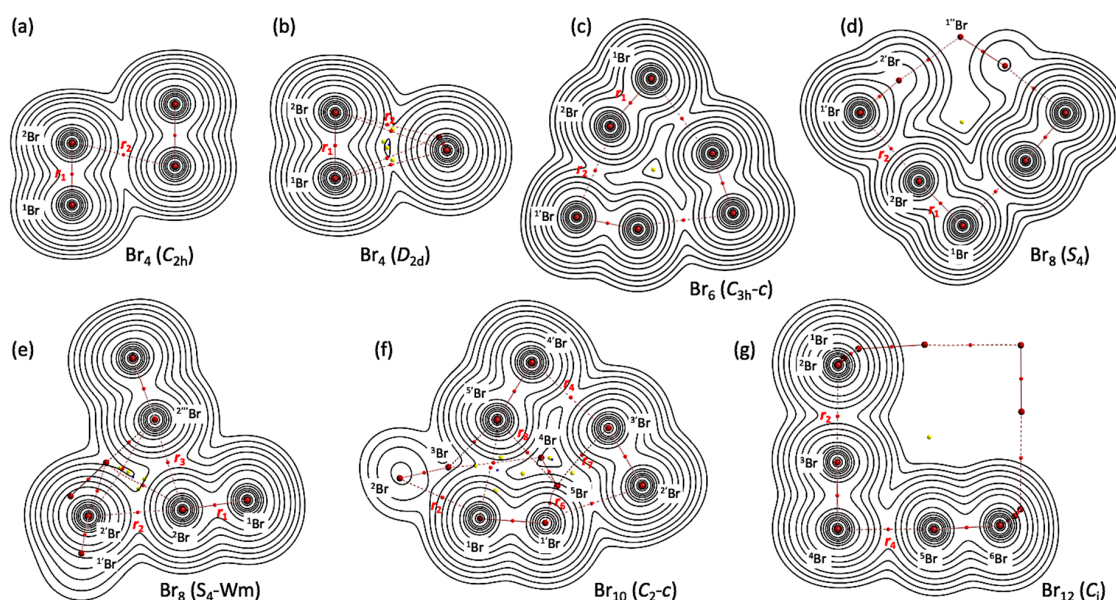

Figure 4. Molecular graphs with contour plots of $\rho(r)$ for the cyclic bromine clusters of Br_4–Br_{12}, (**a**–**g**), calculated with MP2/6-311+G(3df). BCPs are denoted by red dots, RCPs (ring-critical points) by yellow dots, CCPs (cage-critical points) by blue dots, and BPs (bond paths) by pink lines. See ref. [55] for (**a**).

3.3. Survey of the Br-∗-Br Interactions in Polybromine Clusters

As shown in Figures 2–4, the BPs in Br_4–Br_{12} seem almost straight. The linearity is confirmed by comparing the lengths of BPs (r_{BP}) with the corresponding straight-line distances (R_{SL}). The r_{BP} and R_{SL} values are collected in Table S3, together with the differences

between them, Δr_{BP} ($=r_{BP} - R_{SL}$). The magnitudes of Δr_{BP} are less than 0.01 Å, except for r_2 in Br$_4$ (C_{2v}) ($\Delta r_{BP} = 0.014$ Å), r_3 in Br$_8$ (S_4-Wm) (0.014 Å), and r_2 in Br$_{10}$ (C_2-c) (0.012 Å). Consequently, all BPs in Br$_4$–Br$_{12}$ can be approximated as straight lines.

The $\rho_b(r_c)$, $H_b(r_c) - V_b(r_c)/2$ ($=(\hbar^2/8m)\nabla^2\rho_b(r_c)$), and $H_b(r_c)$ values are calculated for the Br-∗-Br interactions at BCPs in the structures of Br$_2$–Br$_{12}$, optimized with MP2/6-311+G(3df) [53–55]. Table 1 collects the values for the noncovalent Br-∗-Br interactions in Br$_4$–Br$_{12}$ of the C_s-L$_m$ type. Table 2 summarizes the values for the noncovalent Br-∗-Br interactions in Br$_4$–Br$_{12}$, other than those of the C_s-L$_m$ type. $H_b(r_c)$ are plotted versus $H_b(r_c) - V_b(r_c)/2$ for the data shown in Tables 1 and 2, together with those from the perturbed structures generated with CIV. Figure 5 shows the plots for the noncovalent Br-∗-Br interactions and covalent Br-∗-Br bonds, exemplified by Br$_{10}$ (C_s-L$_4$).

Table 1. The $\rho_b(r_c)$, $H_b(r_c) - V_b(r_c)/2$ ($=(\hbar^2/8m)\nabla^2\rho_b(r_c)$), and $H_b(r_c)$ values and QTAIM-DFA parameters for Br-∗-Br at BCPs in Br$_4$ (C_s-L$_1$)–Br$_{12}$ (C_s-L$_5$), together with Br$_{10}$ (C_2) and Br$_2$, evaluated with MP2/6-311+G(3df) [1].

Species	BCP on	$\rho_b(r_c)$	$c\nabla^2\rho_b(r_c)$ [2]	$H_b(r_c)$	R [3]	θ [4]
(Symmetry)		(au)	(au)	(au)	(au)	(°)
Br$_4$ (C_s-L$_1$)	r_2	0.0109	0.0045	0.0014	0.0048	72.5
Br$_6$ (C_s-L$_2$)	r_2	0.0113	0.0047	0.0014	0.0049	73.0
Br$_6$ (C_s-L$_2$)	r_4	0.0119	0.0049	0.0014	0.0051	73.7
Br$_8$ (C_s-L$_3$)	r_2	0.0114	0.0047	0.0014	0.0049	73.2
Br$_8$ (C_s-L$_3$)	r_4	0.0124	0.0050	0.0014	0.0052	74.4
Br$_8$ (C_s-L$_3$)	r_6	0.0120	0.0049	0.0014	0.0051	73.9
Br$_{10}$ (C_s-L$_4$)	r_2	0.0114	0.0047	0.0014	0.0049	73.2
Br$_{10}$ (C_s-L$_4$)	r_4	0.0125	0.0051	0.0014	0.0053	74.6
Br$_{10}$ (C_s-L$_4$)	r_6	0.0125	0.0051	0.0014	0.0053	74.6
Br$_{10}$ (C_s-L$_4$)	r_8	0.0120	0.0049	0.0014	0.0051	73.9
Br$_{12}$ (C_s-L$_5$)	r_2	0.0114	0.0047	0.0014	0.0049	73.2
Br$_{12}$ (C_s-L$_5$)	r_4	0.0126	0.0051	0.0014	0.0053	74.7
Br$_{12}$ (C_s-L$_5$)	r_6	0.0127	0.0051	0.0014	0.0053	74.7
Br$_{12}$ (C_s-L$_5$)	r_8	0.0126	0.0051	0.0014	0.0053	74.7
Br$_{12}$ (C_s-L$_5$)	r_{10}	0.0120	0.0049	0.0014	0.0051	73.9
Br$_6$ (C_2)	r_2	0.0104	0.0044	0.0014	0.0046	72.1
Br$_{10}$ (C_2)	r_2	0.0118	0.0048	0.0014	0.0050	73.6
Br$_{10}$ (C_2)	r_4	0.0106	0.0044	0.0014	0.0046	72.3

Species	C_{ii} [5]	$\theta_{p:CIV}$ [6]	$\kappa_{p:CIV}$ [7]	Predicted
(Symmetry)	(Å mdyn^{-1})	(°)	(au^{-1})	nature
Br$_4$ (C_s-L$_1$)	15.311	87.8	121.2	*p*-CS/vdW [8]
Br$_6$ (C_s-L$_2$)	14.984	89.0	124.9	*p*-CS/vdW [8]
Br$_6$ (C_s-L$_2$)	14.114	90.6	127.3	*p*-CS/*t*-HB [9]
Br$_8$ (C_s-L$_3$)	14.826	89.2	125.0	*p*-CS/vdW [8]
Br$_8$ (C_s-L$_3$)	13.590	92.2	132.0	*p*-CS/*t*-HB [9]
Br$_8$ (C_s-L$_3$)	14.048	90.9	127.1	*p*-CS/*t*-HB [9]
Br$_{10}$ (C_s-L$_4$)	14.751	89.4	126.2	*p*-CS/vdW [8]
Br$_{10}$ (C_s-L$_4$)	13.445	92.6	133.2	*p*-CS/*t*-HB [9]
Br$_{10}$ (C_s-L$_4$)	13.478	92.6	132.5	*p*-CS/*t*-HB [9]
Br$_{10}$ (C_s-L$_4$)	13.983	91.1	128.4	*p*-CS/*t*-HB [9]
Br$_{12}$ (C_s-L$_5$)	14.719	89.5	126.9	*p*-CS/vdW [8]
Br$_{12}$ (C_s-L$_5$)	13.376	92.7	133.3	*p*-CS/*t*-HB [9]
Br$_{12}$ (C_s-L$_5$)	13.334	93.0	134.3	*p*-CS/*t*-HB [9]
Br$_{12}$ (C_s-L$_5$)	13.393	92.8	132.6	*p*-CS/*t*-HB [9]
Br$_{12}$ (C_s-L$_5$)	13.962	91.1	128.8	*p*-CS/*t*-HB [9]
Br$_6$ (C_2)	16.025	86.7	119.2	*p*-CS/vdW [8]
Br$_{10}$ (C_2)	14.218	90.2	126.7	*p*-CS/*t*-HB [9]
Br$_{10}$ (C_2)	16.378	87.2	120.0	*p*-CS/vdW [8]

[1] The interactions in minima are shown. [2] $c\nabla^2\rho_b(r_c) = H_b(r_c) - V_b(r_c)/2$, where $c = \hbar^2/8m$. [3] $R = [(H_b(r_c) - V_b(r_c)/2)^2 + H_b(r_c)^2]^{1/2}$. [4] $\theta = 90° - \tan^{-1}[H_b(r_c)/(H_b(r_c) - V_b(r_c)/2)]$. [5] Defined in Equation (R1) in the text. [6] $\theta_p = 90° - \tan^{-1}(\mathrm{d}y/\mathrm{d}x)$, where $(x, y) = (H_b(r_c) - V_b(r_c)/2, H_b(r_c))$. [7] $\kappa_p = |\mathrm{d}^2y/\mathrm{d}x^2|/[1 + (\mathrm{d}y/\mathrm{d}x)^2]^{3/2}$. [8] The *pure* CS interaction of the vdW nature. [9] The *pure* CS interaction of the HB nature without covalency.

Table 2. The $\rho_b(r_c)$, $H_b(r_c) - V_b(r_c)/2$ $(=(\hbar^2/8m)\nabla^2\rho_b(r_c))$, and $H_b(r_c)$ values and QTAIM-DFA parameters for Br-∗-Br at BCPs in Br_4–Br_{12}, other than the C_s-L_m structures, evaluated with MP2/6-311+G(3df) [1].

Species	BCP on	$\rho_b(r_c)$	$c\nabla^2\rho_b(r_c)$ [2]	$H_b(r_c)$	R [3]	θ [4]
(Symmetry)		(au)	(au)	(au)	(au)	(°)
Br_4 (C_{2h})	r_2	0.0055	0.0022	0.0009	0.0024	67.2
Br_4 (D_{2d})	r_2	0.0042	0.0017	0.0007	0.0018	66.0
Br_6 (C_{3h}-c)	r_2	0.0092	0.0038	0.0013	0.0040	70.7
Br_8 (S_4)	r_2	0.0128	0.0051	0.0014	0.0053	74.8
Br_8 (S_4-Wm) [5]	r_2	0.0136	0.0054	0.0013	0.0056	76.0
Br_8 (S_4-Wm) [5]	r_3	0.0038	0.0015	0.0007	0.0016	66.0
Br_{10} (C_2-c)	r_2	0.0087	0.0035	0.0012	0.0037	70.5
Br_{10} (C_2-c)	r_4	0.0097	0.0040	0.0014	0.0042	71.3
Br_{10} (C_2-c)	r_6	0.0110	0.0044	0.0014	0.0046	73.0
Br_{10} (C_2-c)	r_7	0.0049	0.0019	0.0008	0.0021	66.2
Br_{10} (C_2-c)	r_8	0.0049	0.0018	0.0008	0.0020	66.6
Br_{12} (C_i)	r_2	0.0129	0.0052	0.0014	0.0054	75.0
Br_{12} (C_i)	r_4	0.0129	0.0052	0.0014	0.0054	75.0

Species	C_{ii} [6]	$\theta_{p:CIV}$ [7]	$\kappa_{p:CIV}$ [8]	Predicted
(Symmetry)	(Å mdyn^{-1})	(°)	(au^{-1})	nature
Br_4 (C_{2h})	24.709	73.6	122.9	p-CS/vdW [9]
Br_4 (D_{2d})	40.402	69.6	136.3	p-CS/vdW [9]
Br_6 (C_{3h}-c)	25.617	83.3	121.7	p-CS/vdW [9]
Br_8 (S_4)	13.201	93.5	139.2	p-CS/t-HB [10]
Br_8 (S_4-Wm) [5]	11.294	95.3	139.0	p-CS/t-HB [10]
Br_8 (S_4-Wm) [5]	52.918	67.5	204.0	p-CS/vdW [9]
Br_{10} (C_2-c)	34.402	81.3	112.7	p-CS/vdW [9]
Br_{10} (C_2-c)	23.971	84.7	122.1	p-CS/vdW [9]
Br_{10} (C_2-c)	20.831	87.6	122.6	p-CS/vdW [9]
Br_{10} (C_2-c)	29.570	71.5	118.9	p-CS/vdW [9]
Br_{10} (C_2-c)	37.855	71.8	120.4	p-CS/vdW [9]
Br_{12} (C_i)	13.483	93.7	137.9	p-CS/t-HB [10]
Br_{12} (C_i)	13.482	93.7	137.3	p-CS/t-HB [10]

[1] The interactions in minima are shown. [2] $c\nabla^2\rho_b(r_c) = H_b(r_c) - V_b(r_c)/2$, where $c = \hbar^2/8m$. [3] $R = [H_b(r_c) - V_b(r_c)/2)^2 + H_b(r_c)^2]1/2$. [4] $\theta = 90° - \tan^{-1}[H_b(r_c)/(H_b(r_c) - V_b(r_c)/2)]$. [5] Image from windmill. [6] Defined in Equation (R1) in the text. [7] $\theta_p = 90° - \tan^{-1}(dy/dx)$, where $(x, y) = (H_b(r_c) - V_b(r_c)/2, H_b(r_c))$. [8] $\kappa_p = |\,d^2y/dx^2\,|/[1 + (dy/dx)^2]^{3/2}$. [9] The *pure* CS interaction of the vdW nature. [10] The *pure* CS interaction of the HB nature without covalency.
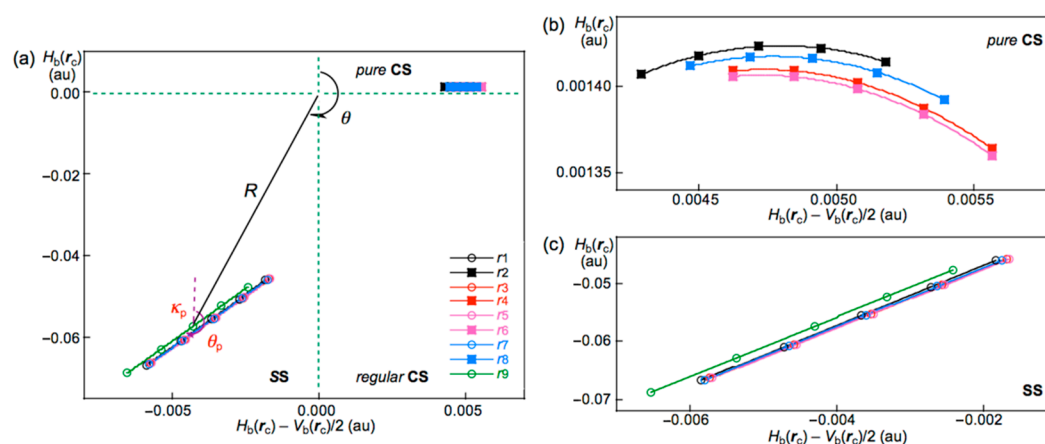

Figure 5. QTAIM-DFA plots ($H_b(r_c)$ versus $H_b(r_c) - V_b(r_c)/2$) for the interactions in Br_{10} (C_s-L_4), evaluated with MP2/6-311+G(3df); (**a**) whole region, (**b**) *pure* CS region, and (**c**) SS region. Marks and colors are shown in the figure.

QTAIM-DFA parameters of (R, θ) and (θ_p, κ_p) are obtained by analyzing the plots of $H_b(r_c)$ versus $H_b(r_c) - V_b(r_c)/2$, according to Equations (S3)–(S6). Table 1 collects the QTAIM-DFA parameters for the noncovalent Br-∗-Br interactions of Br_4 (C_s-L_1)–Br_{12} (C_s-L_5), Br_6 (C_2), and Br_{10} (C_2) together with the C_{ii} values. Table 2 collects the (R, θ) and (θ_p, κ_p) values for Br_4–Br_{12}, other than those given in Table 1, together with the C_{ii} values. The (R, θ) and (θ_p, κ_p) values for the covalent Br-∗-Br bonds in Br_4–Br_{12} are collected in Table S4.

3.4. The Nature of Br-∗-Br Interactions in Polybromine Clusters

The nature of the covalent and noncovalent Br-∗-Br interactions in Br_2–Br_{12} is discussed on the basis of the (R, θ, θ_p) values, employing standard values as a reference (see Scheme SA3).

It is instructive to survey the criteria shown in Scheme SA3 before detailed discussion. The criteria tell us that $180° < \theta$ ($H_b(r_c) - V_b(r_c)/2 < 0$) for the SS interactions and $\theta < 180°$ ($H_b(r_c) - V_b(r_c)/2 > 0$) for the CS interactions. The CS interactions are subdivided into *pure* CS interactions (*p*-CS) of $45° < \theta < 90°$ ($H_b(r_c) > 0$) and *regular* CS interactions (*r*-CS) of $90° < \theta < 180°$ ($H_b(r_c) < 0$). The θ_p value predicts the character of interactions. In the *pure* CS region of $45° < \theta < 90°$, the character of interactions will be the vdW type for $45° < \theta_p < 90°$ and the *typical*-HB type with no covalency (*t*-HB$_{nc}$) for $90° < \theta_p < 125°$, where $\theta_p = 125°$ approximately corresponds to $\theta = 90°$. The classical chemical covalent bonds of SS ($180° < \theta$) will be strong when $R > 0.15$ au (Cov-s: strong covalent bonds), whereas they will be weak for $R < 0.15$ au (Cov-w: weak covalent bonds).

The (R, θ, θ_p) values are (0.0576 au, 184.3°, 190.9°) for the original Br_2 if evaluated with MP2/6-311+G(3df). Therefore, the nature of the Br-∗-Br bond in Br_2 is classified by the SS interactions ($\theta > 180°$) and characterized to have a Cov-w nature ($\theta_p > 180°$ and $R < 0.15$ au). The nature is denoted by SS/Cov-w. The (R, θ, θ_p) values for the covalent Br-∗-Br bonds in Br_4–Br_{12} are (0.0472–0.0578 au, 182.0–184.4°, 190.4–192.1°); therefore, their nature is predicted to be SS/Cov-w. The nature of the covalent Br-∗-Br bonds seems unchanged in the formation of the clusters [53,54]. The noncovalent Br-∗-Br interactions in Br_4–Br_{12} are all classified by *pure* CS interactions since $\theta \leq 76°$ ($\ll 90°$) [53,54]. The θ_p values in the C_s-L_m clusters change systematically. The θ_p values for r_2 in Br_{2k} (C_s-L_m) (k = 2–6) are predicted to be in the range of $89.1° \leq \theta_p \leq 89.6°$, with $\theta_p = 87.9°$ for Br_4 (C_s-L_1).

However, the values for r_{n-2} in Br_{2k} (C_s-L_m) (k = 2–6) are in the range of $90.6° \leq \theta_p \leq 91.2°$ and the values for noncovalent interactions, other than edge positions, are in the range of $92.1° \leq \theta_p \leq 93.0°$. Namely, the noncovalent Br-∗-Br interactions are predicted to have the vdW nature (*p*-CS/vdW) for r_2, while the interactions other than r_2 are predicted to have the *t*-HB$_{nc}$ nature (*p*-CS/*t*-HB$_{nc}$) since $\theta_p > 90°$. The θ_p values of r_2 for the C_s-L_m clusters will be less than 90°, irrespective of the angles between r_1 and r_2, which are close to 180°. The θ_p values will be larger than 90° for all noncovalent interactions other than r_2. Table 1 contains the data for Br_{10} (C_2), of which $\theta_p = 90.4°$ ($> 90°$) for r_2 and $\theta_p = 87.1°$ ($< 90°$) for r_4, although Br_{10} (C_2) is not the C_s-L_m type. The results for r_2 seem reasonable based on the structure (cf. Figure 3), while those for r_4 would be complex. Table 1 summarizes the predicted nature.

In the case of the noncovalent Br-∗-Br interactions in Br_4–Br_{12}, other than the C_s-L_m type clusters, $\theta_p > 90°$ for r_2 in Br_8 (S_4) ($\theta_p = 93.4°$) and Br_8 (S_4-Wm) ($\theta_p = 94.8°$) and for r_2, r_4, and r_6 in Br_{12} (C_i) ($93.4° \leq \theta_p \leq 93.7°$). The interactions would have the *t*-HB$_{nc}$ nature (*p*-CS/*t*-HB$_{nc}$). Very weak noncovalent Br-∗-Br interactions are also detected. The ranges of $64.2° \leq \theta \leq 66.6°$ and $66.2° \leq \theta_p \leq 71.2°$ are predicted for r_2 and r_3 in Br_4 (C_{2h}), r_2 in Br_4 (C_{2v}), r_3 in Br_8 (S_4-Wm), and r_7 and r_8 in Br_{10} (C_2-c). The results are summarized in Table 2.

What are the relationships between the QTAIM-DFA parameters for the noncovalent Br-∗-Br interactions? The θ and θ_p values are plotted versus R. The plots are shown in Figure S4; they give very good correlations. The θ_p values are plotted versus θ. The plot is shown in Figure S5; it also gives a very good correlation. Table 3 summarizes the correlations among the QTAIM-DFA parameters.

Table 3. Correlations in the plots [1].

Entry	Correlation	*a*	*b*	R_c^2	*n*
1	ΔE_{ZP} vs. ΔE_{ES}	0.940	0.129	0.9999	20 [2]
2	θ vs. R	2595.6	60.70	0.979	33
3	θ_p vs. R	6449.1	58.19	0.989	33
4	θ_p vs. θ	2.67	−106.26	0.992	31 [3]
5	$E(2)$ vs. C_{ii}^{-1}	535.5	−18.22	0.997	15 [4]
6	$E(2)$ vs. R	9760.9	−29.92	0.983	15 [4]
7	$E(2)$ vs θ	2.446	−160.88	0.996	15 [4]
8	$E(2)$ vs. θ_p	1.067	77.17	0.999	15 [4]

[1] The constants (a, b, R_c^2) are the correlation constant, the *y*-intercept, and the square of the correlation coefficient, respectively, in $y = ax + b$. [2] Containing TS species. [3] Neglecting the data of r_2 and r_3 in Br_4 (C_{2h}). [4] For the noncovalent Br-∗-Br interactions in Br_4 (C_s-L_1)–Br_{12} (C_s-L_5).

To further examine the behavior of noncovalent Br-∗-Br interactions, NBO analysis is applied to the interactions.

3.5. NBO Analysis for Br-∗-Br of Br_4 (C_s-L_1)–Br_{12} (C_s-L_5)

The noncovalent Br-∗-Br interactions in Br_4(C_s-L_1)–Br_{12} (C_s-L_5) are characterized by σ(3c–4e) of the n(Br)→σ*(Br–Br) type. NBO analysis [56] was applied to the n(Br)→σ*(Br–Br) interactions with MP2/6-311+G(3df). For each donor NBO (*i*) and acceptor NBO (*j*), the stabilization energy $E(2)$ is calculated based on the second-order perturbation theory in NBO. The $E(2)$ values are calculated according to Equation (4), where q_i is the donor orbital occupancy, ε_i, ε_j are diagonal elements (orbital energies), and $F(i,j)$ is the off-diagonal NBO Fock matrix element. The values are obtained separately by the contributions from n_s(Br)→σ*(Br–Br) and n_p(Br)→σ*(Br–Br), which are summarized in Table S5. The total values corresponding to n_{s+p}(Br)→σ*(Br–Br) (=n_s(Br)→σ*(Br–Br) + n_p(Br)→σ*(Br–Br)) were calculated, which are also summarized in Table S5. The total values are employed for the discussion.

$$E(2) = q_i \times F(i,j)^2 / (\varepsilon_j - \varepsilon_i) \tag{4}$$

Figure 6 shows the plots of $E(2)$ and θ_p for the noncovalent Br-∗-Br interactions in Br_4 (C_s-L_1)–Br_{12} (C_s-L_5). The values become larger in the order of P (r_2: Br_4 (C_s-L_1)) < P (r_2: Br_6 (C_s-L_2)–Br_{12} (C_s-L_5)) < P (r_ω: Br_6 (C_s-L_2)–Br_{12} (C_s-L_5)) < P (r_{in}: Br_6 (C_s-L_2)–Br_{12} (C_s-L_5)), where P means $E(2)$ or θ_p, while r_ω and r_{in} stand for the last end and the inside noncovalent interactions, respectively, in the sequence (see Figures 2 and 3). The values for P = $E(2)$ are as follows: $E(2)$ = 16.6 kJ mol^{-1} for r_2 in Br_4 (C_s-L_1) < 17.7 ≤ $E(2)$ ≤ 18.2 kJ mol^{-1} for r_2 in Br_6 (C_s-L_2)–Br_{12} (C_s-L_5) < 19.5 ≤ $E(2)$ ≤ 20.0 kJ mol^{-1} for r_ω in Br_6 (C_s-L_2)– Br_{12} (C_s-L_5) < 21.2 ≤ $E(2)$ ≤ 22.0 kJ mol^{-1} for r_{in} in Br_8 (C_s-L_3)–Br_{12} (C_s-L_5).

Relations between $E(2)$ and C_{ii} were also examined for noncovalent Br-∗-Br interactions in Br_4 (C_s-L_1)–Br_{12} (C_s-L_5). The $E(2)$ values were plotted versus C_{ii}^{-1} for the noncovalent interactions. Figure 7 shows the plot. The plot gives a very good correlation, which is shown in Table 3 (Entry 5). The results show that the energies for σ(3c–4e) of the n_p(Br)→σ*(Br–Br) type in Br_4 (C_s-L_1)–Br_{12} (C_s-L_5) are well evaluated, not only by $E(2)$ but also by C_{ii}^{-1}. Similar relations would be essentially observed for the interactions in the nonlinear clusters; however, the analyses will be much complex due to the unsuitable structures for the NBO analysis, such as the deviations in the interaction angles expected for Br_3 σ(3c–4e), the mutual interactions between Br_3 σ(3c–4e), and/or the steric effect from other bonds and interactions, placed proximity in space. The $E(2)$ values for Br_4 (C_s-L_1)–Br_{12} (C_s-L_5) were also plotted versus R, θ, and θ_p, shown in Figures S6–S8, respectively. The plots give very good correlations, which are given in Table 3 (Entries 6–8).

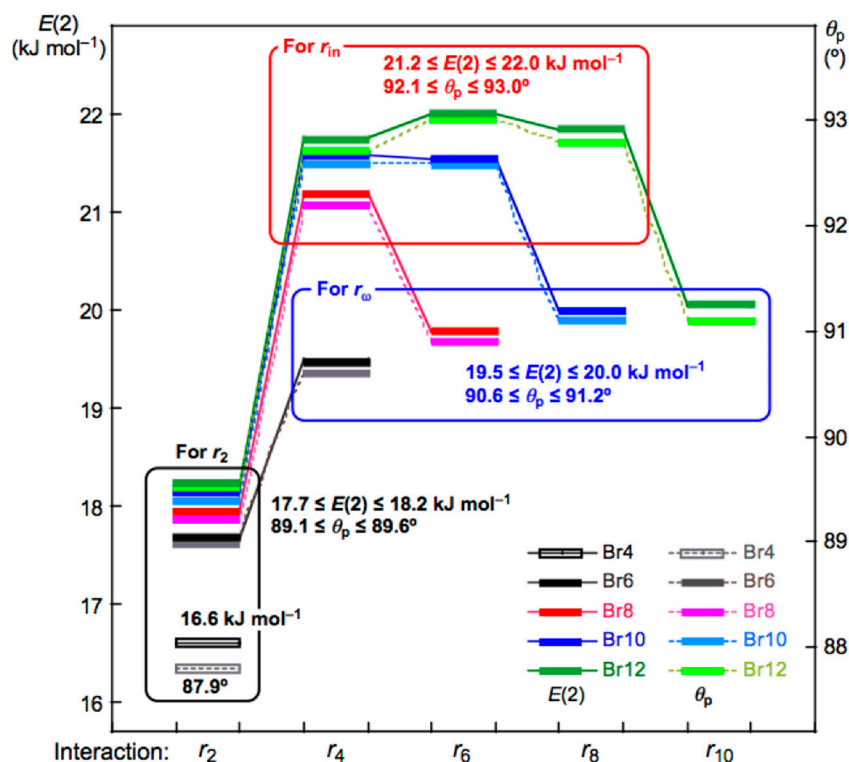**Figure 6.** Plots of θ_p and $E(2)$ for the noncovalent Br-∗-Br interactions in Br$_4$ (C_s-L$_1$)–Br$_{12}$ (C_s-L$_5$). Colors are shown in the figure.
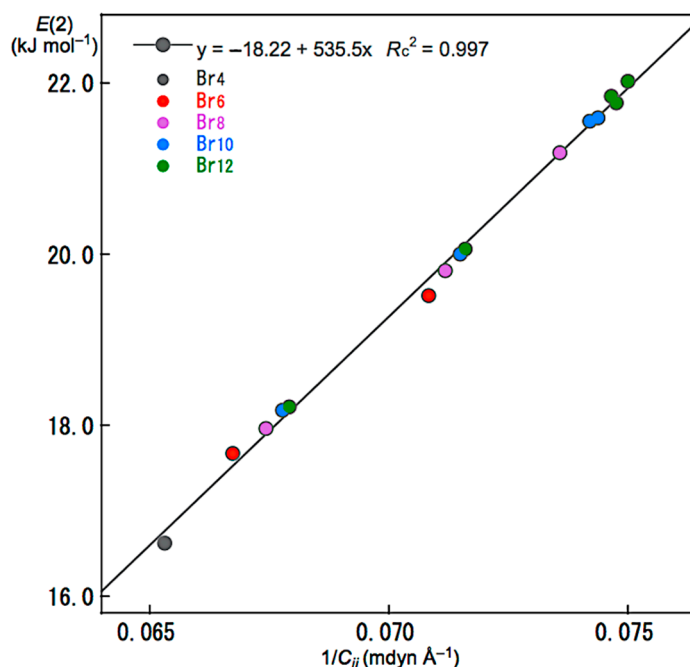
Figure 7. Plot of $E(2)$ versus $1/C_{ii}$ for the noncovalent Br-∗-Br interactions in Br$_4$ (C_s-L$_1$)–Br$_{12}$ (C_s-L$_5$).

3.6. MO Descriptions for Noncovalent Br-∗-Br Interactions in Br$_4$

As discussed above, Br$_3$ σ(3c–4e) of the n_p(Br)→σ*(Br–Br) type plays an important role in the formation of Br$_4$ (C_s-L$_1$)–Br$_{12}$ (C_s-L$_5$). However, there must exist some interactions, other than Br$_3$ σ(3c–4e), to stabilize the clusters. The ΔE_{ES} values for Br$_4$ (C_{2h}) (−8.0 kJ mol^{-1}) and Br$_4$ (D_{2d}) (−9.1 kJ mol^{-1}) are not so different from that for Br$_4$ (C_s-L$_1$) (−10.7 kJ mol^{-1}). However, Br$_4$ (C_{2h}) and Br$_4$ (D_{2d}) must consist of interactions other than

σ(3c–4e). Indeed, Br_3 σ(3c–4e) of the $n(Br) \rightarrow \sigma^*(Br–Br)$ type contributes to stabilizing Br_4 (C_s-L_1), but Br_4 (C_{2h}) and Br_4 (D_{2d}) are shown to be stabilized by the σ(Br–Br)$\rightarrow \sigma^*$Ry(Br) interaction by NBO, where Ry stands for the Rydberg term, although not shown.

The total energy for a species (E) is given by the sum of the core terms ($H_c(i)$) over all electrons, $\Sigma_i^n H_c(i)$, and the electron–electron repulsive terms, $(\Sigma_{i \neq j}^n J_{ij} - \Sigma_{i \neq j,\|}^n K_{ij})/2$, as shown by Equation (5), where $H_c(i)$ consists of the kinetic energy and electron–nuclear attractive terms for electron i. E contains the nuclear–nuclear repulsive terms, although not clearly shown in Equation (5). As shown in Equation (6), the sum of MO energy for electron i, ε_i, over all electrons, $\Sigma_{i=1}^n \varepsilon_i$, will be larger than E by $(\Sigma_{i \neq j}^n J_{ij} - \Sigma_{i \neq j,\|}^n K_{ij})/2$ since the electron–electron repulsions are doubly counted in Equation (6). Therefore, $\Sigma_i^n H_c(i)$ and $(\Sigma_{i \neq j}^n J_{ij} - \Sigma_{i \neq j,\|}^n K_{ij})/2$ are given separately by Equations (7) and (8), respectively. The ε_i values for Br_4 (C_{2h}), Br_4 (D_{2d}), and $2Br_2$, together with Br_4 (C_s-L_1), are collected in Tables S6–S9, respectively, for convenience of discussion. Parameters (ΔP) in the formation of Br_{2k} from the components are evaluated according to Equation (9). The $\Delta\Sigma_i^n H_c(i)$ and $\Delta(\Sigma_{i \neq j}^n J_{ij} - \Sigma_{i \neq j,\|}^n K_{ij})/2$ values for the formation of Br_4 (C_{2h}), Br_4 (D_{2d}), and Br_4 (C_s-L_1) are collected in Table S11.

$$E = \Sigma_i^n H_c(i) + (\Sigma_{i \neq j}^n J_{ij} - \Sigma_{i \neq j,\|}^n K_{ij})/2 \tag{5}$$

$$\Sigma_{i=1}^n \varepsilon_i = \Sigma_i^n H_c(i) + (\Sigma_{i \neq j}^n J_{ij} - \Sigma_{i \neq j,\|}^n K_{ij}) \tag{6}$$

$$\Sigma_i^n H_c(i) = 2E - \Sigma_{i=1}^n \varepsilon_i \tag{7}$$

$$(\Sigma_{i \neq j}^n J_{ij} - \Sigma_{i \neq j,\|}^n K_{ij})/2 = \Sigma_{i=1}^n \varepsilon_i - E \tag{8}$$

$$\Delta P(Br_{2k}) = P(Br_{2k}) - kP(Br_2) \tag{9}$$

The nature of noncovalent Br—Br interactions in Br_4 (C_s-L_1) is examined first. The σ(3c–4e) character in Br_4 (C_s-L_1) is confirmed by the natural charge evaluated with NPA (Qn), developed in the formation of Br_4 (C_s-L_1). The evaluated Qn values are Br(1: $-0.0128\,|e^-|$)–Br(2: $-0.0002\,|e^-|$)—Br(3: $-0.0010\,|e^-|$)–Br(4: $0.0140\,|e^-|$); therefore, Qn(Br(4)–Br(3)) and Qn(Br(2)–Br(1)) are $+0.013\,|e^-|$ and $-0.013\,|e^-|$, respectively. Each MO in Br_4 (C_s-L_1) is almost localized on Br(4)–Br(3) or Br(2)–Br(1), except for a few cases. MOs in Br_4 (C_s-L_1) must be affected by the local charge. Each MO energy in Br_4 (C_s-L_1) seems higher than the corresponding value of $2Br_2$ by 10–20 kJ mol^{-1} if the MO is localized on Br(2)–Br(1), lower by 15–25 kJ mol^{-1} on Br(3)–Br(4), and slightly lower by 0–5 kJ mol^{-1} if the MO is localized on the whole molecule. We should be careful since it depends on the phase in MO and the position of the Br atom(s). Typical cases are shown in Figure S9. In total, $\Delta\Sigma_{i=1}^n \varepsilon_i$ is evaluated to be -357.2 kJ mol^{-1} for Br_4 (C_s-L_1). The results show that Br_4 (C_s-L_1) is stabilized in the formation of the dimer from the components through the lowering of MO energies in total, which is consistent with those evaluated with NBO, as discussed above.

Figure 8 shows the plots of $\Delta\Sigma_i^n H_c(i)$ and $\Delta(\Sigma_{i \neq j}^n J_{ij} - \Sigma_{i \neq j,\|}^n K_{ij})/2$ for Br_4 (C_s-L_1), Br_4 (C_{2h}), and Br_4 (D_{2d}), together with ΔE_{ES} and $\Delta\Sigma_{i=1}^n \varepsilon_i$. In the case of Br_4 (C_s-L_1), $\Delta\Sigma_i^n H_c(i)$ and $\Delta(\Sigma_{i \neq j}^n J_{ij} - \Sigma_{i \neq j,\|}^n K_{ij})/2$ are evaluated to be 335.7 and -346.4 kJ mol^{-1}, respectively, which stabilizes Br_4 (C_s-L_1) in total. Two Br_2 molecules in Br_4 (C_s-L_1) will supply a wider area for electrons without severe disadvantageous steric compression by the L-shaped structure in a plane. The structural feature of Br_4 (C_s-L_1) may reduce (or may not severely increase) the electron–electron repulsive terms, $\Delta((\Sigma_{i \neq j}^n J_{ij} - \Sigma_{i \neq j,\|}^n K_{ij})/2)$, relative to the case of $2Br_2$, although $\Delta\Sigma_i^n H_c(i)$ seems to destabilize it. The $\Delta\Sigma_i^n H_c(i) + \Delta(\Sigma_{i \neq j}^n J_{ij} - \Sigma_{i \neq j,\|}^n K_{ij})/2$ value is equal to -10.7 kJ mol^{-1}, which corresponds to the stabilization energy of Br_4 (C_s-L_1), relative to $2Br_2$.
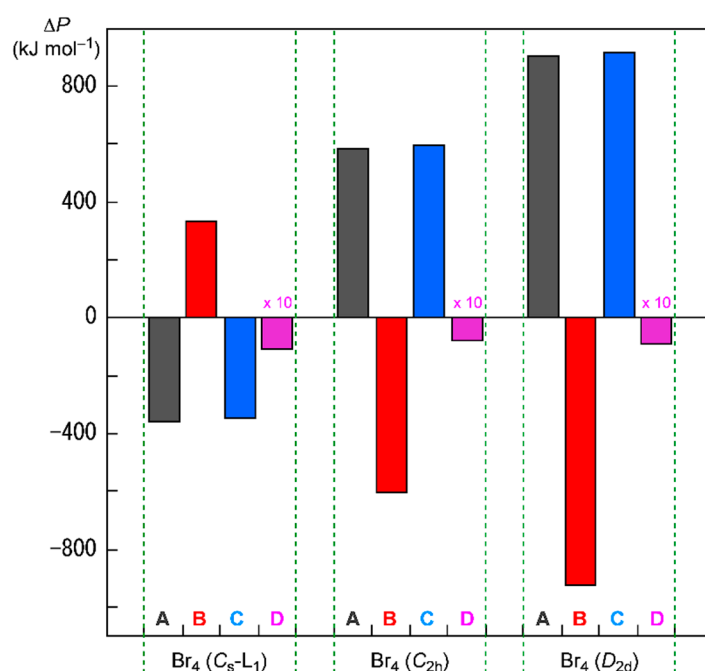
Figure 8. Contributions from $\Delta\Sigma_i^{\,n} H_c(i)$ ($=\Delta P = \mathbf{B}$) and $\Delta(\Sigma_{i\neq j}^{\,n} J_{ij} - \Sigma_{i\neq j,\|}^{\,n} K_{ij})/2$ ($=\Delta P = \mathbf{C}$) to ΔE_{ES} ($=\Delta P = \mathbf{D}$, magnified by 10 times in the plot) for Br_4 (C_s-L_1), Br_4 (C_{2h}), and Br_4 (D_{2d}), relative to $2Br_2$, together with $\Delta\Sigma_{i=1}^{\,n} \varepsilon_i$ ($=\Delta P = \mathbf{A}$).

The energy profiles of Br_4 (C_{2h}) and Br_4 (D_{2d}) seem very different from that of Br_4 (C_s-L_1). The $\Delta\Sigma_{i=1}^{\,n} \varepsilon_i$ terms for Br_4 (C_{2h}) and Br_4 (D_{2d}) are evaluated to be 587.5 and 908.1 kJ mol^{-1}, respectively. Namely, Br_4 (C_{2h}) and Br_4 (D_{2d}) would be less stable than $2Br_2$ if $\Delta\Sigma_{i=1}^{\,n} \varepsilon_i$ are compared. Consequently, it is difficult to explain the stability of Br_4 (C_{2h}) and Br_4 (D_{2d}), based on the MO energies. On the other hand, $\Delta\Sigma_i^{\,n} H_c(i)$ of Br_4 (C_{2h}) and Br_4 (D_{2d}) are evaluated to be -603.5 and -926.3 kJ mol^{-1}, respectively, whereas $\Delta(\Sigma_{i\neq j}^{\,n} J_{ij} - \Sigma_{i\neq j,\|}^{\,n} K_{ij})/2$ are 595.5 and 917.2 kJ mol^{-1}, respectively. As a result, the ($\Delta\Sigma_i^{\,n} H_c(i) + \Delta(\Sigma_{i\neq j}^{\,n} J_{ij} - \Sigma_{i\neq j,\|}^{\,n} K_{ij})/2$) values are -8.0 and -9.1 kJ mol^{-1} for Br_4 (C_{2h}) and Br_4 (D_{2d}), respectively, which correspond to their ΔE_{ES} values (relative to $2E(Br_2)$). The results show that the stabilizing effect of $\Delta\Sigma_i^{\,n} H_c(i)$ overcomes the shorter electron–nuclear distances in the species on average. The shorter electron–electron distances must destabilize Br_4 (C_{2h}) and Br_4 (D_{2d}) through the factor of $\Delta(\Sigma_{i\neq j}^{\,n} J_{ij} - \Sigma_{i\neq j,\|}^{\,n} K_{ij})/2$, which is the inverse effect from the electron–nuclear interaction on $\Delta\Sigma_i^{\,n} H_c(i)$. However, the effect of the shorter distances on $\Delta\Sigma_i^{\,n} H_c(i)$ seems to contribute more effectively than the case of $\Delta(\Sigma_{i\neq j}^{\,n} J_{ij} - \Sigma_{i\neq j,\|}^{\,n} K_{ij})/2$ in Br_4 (C_{2h}) and Br_4 (D_{2d}), although they are not so large.

How can the BPs in Br_4 (C_{2h}) and Br_4 (D_{2d}) be rationalized through orbital interactions? The $\Delta\varepsilon_i$ values of Br_4 (C_{2h}) are positive for all occupied MOs, relative to the corresponding values of $2Br_2$, except for HOMO-3 (-5.5 kJ mol^{-1}), HOMO-6 (-2.9 kJ mol^{-1}), HOMO-7 (-35.8 kJ mol^{-1}), and HOMO-13 (-1.1 kJ mol^{-1}). Figure 9 illustrates the interactions to produce HOMO, HOMO-3, HOMO-4, and HOMO-7. Indeed, HOMO-7 seems to contribute well to stabilizing Br_4 (C_{2h}), but HOMO-4 ($+40.8$ kJ mol^{-1}) is also formed in the $\pi(Br_2)$–$\pi(Br_2)$ mode. Similarly, HOMO ($+13.7$ kJ mol^{-1}) is formed, together with HOMO-3 in the $\pi^*(Br_2) + \pi^*(Br_2)$ mode. Therefore, all MOs seem not to contribute to stabilizing Br_4 (C_{2h}) inherently. Nevertheless, HOMO, HOMO-4, and HOMO-7 seem to rationalize the appearance of BPs in Br_4 (C_{2h}), along the diagonal line and shorter sides of the parallelogram, although all electrons contribute to the appearance of BPs in molecules.
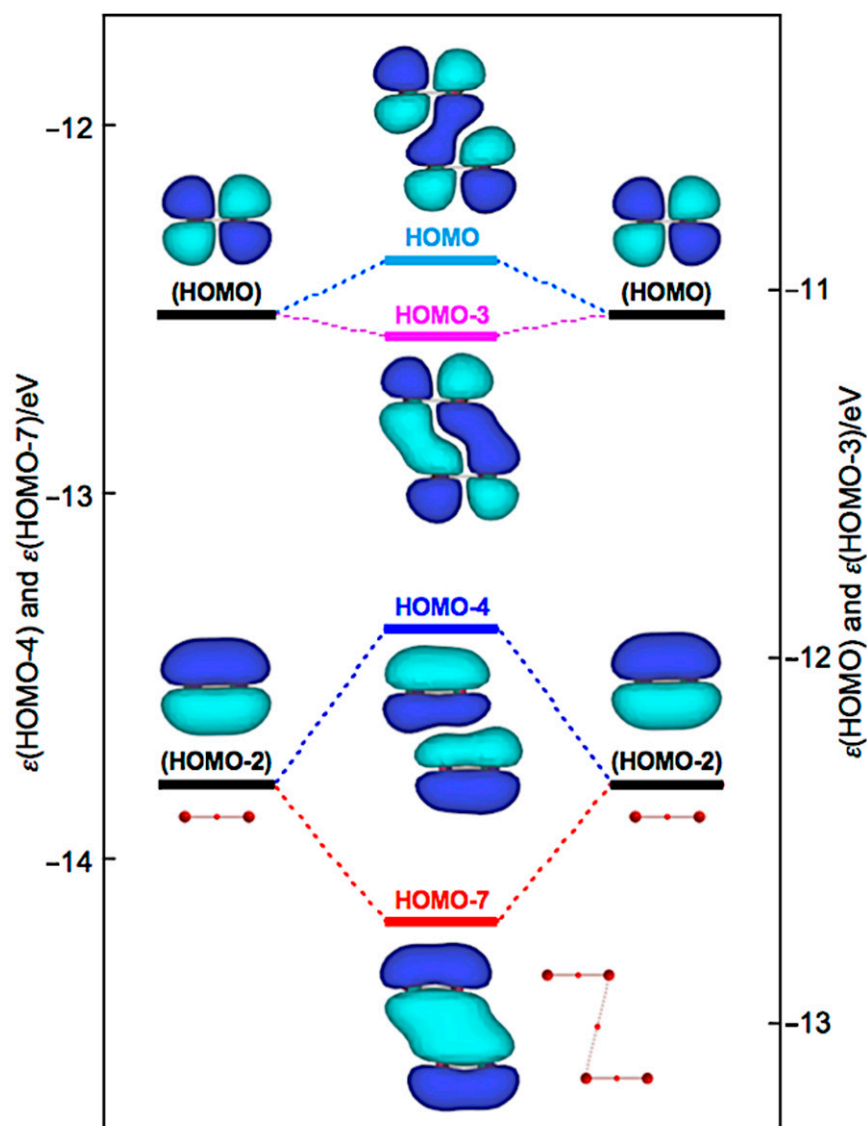
Figure 9. Energy profile for the formation of Br$_4$ (C_{2h}), exemplified by HOMO, HOMO-3, HOMO-4, and HOMO-7.

Similarly, $\Delta \varepsilon_i$ of Br$_4$ (D_{2d}) are positive for all occupied MOs, relative to the corresponding values of 2Br$_2$, except for HOMO-3 (-1.9 kJ mol^{-1}), HOMO-7 (-39.2 kJ mol^{-1}), and HOMO-13 (-0.5 kJ mol^{-1}). Figure 10 illustrates the interactions to produce HOMO, HOMO-3, HOMO-4, and HOMO-7 in Br$_4$ (D_{2d}). HOMO-4 ($+50.2$ kJ mol^{-1}) is formed through the π(Br$_2$)–π(Br$_2$) mode in addition to HOMO-7. Similarly, HOMO ($+13.9$ kJ mol^{-1}) is formed, accompanied by HOMO-3, in the π^*(Br$_2$) + π^*(Br$_2$) mode. Therefore, no MOs essentially stabilize Br$_4$ (D_{2d}). However, the appearance of BPs along the longer and shorter diagonal lines of the tetrahedron of Br$_4$ (D_{2d}) seem to be rationalized by HOMO-7, together with HOMO-3 and HOMO-4, modifying the BPs, although BPs will appear as the whole properties of molecules.
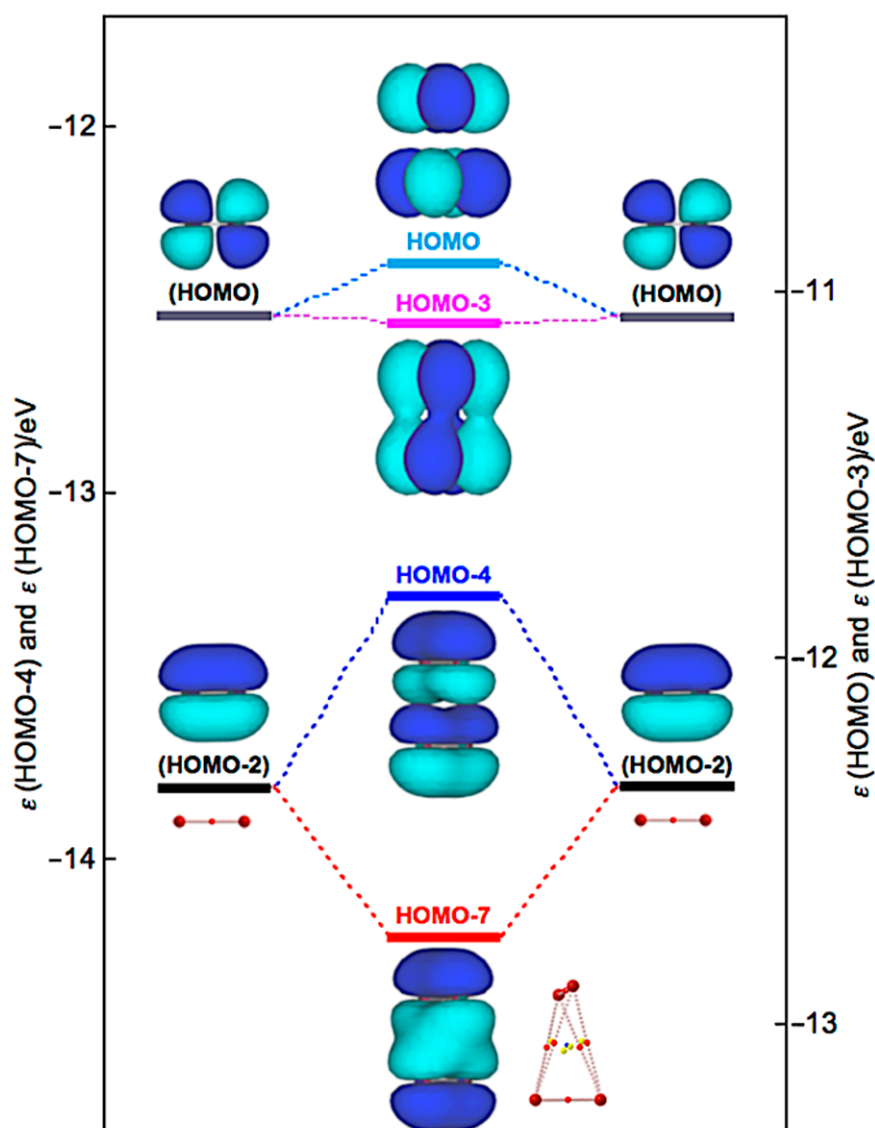
Figure 10. Energy profile for the formation of Br_4 (D_{2d}), exemplified by HOMO, HOMO-3, HOMO-4, and HOMO-7.

The nature of interactions in the charged clusters is also of interest. Such investigations are in progress.

4. Conclusions

The intrinsic dynamic and static nature of noncovalent Br-∗-Br interactions was elucidated for Br_4–Br_{10} with MP2/6-311+G(3df). QTAIM-DFA was applied to the investigation. $H_b(r_c)$ were plotted versus $H_b(r_c) - V_b(r_c)/2$ for the interactions at BCPs of the fully optimized structures, together with those from the perturbed structures, generated with CIV. The nature of the covalent Br-∗-Br bonds in Br_4–Br_{10} is predicted to have the SS/Cov-w nature if calculated with MP2/6-311+G(3df). On the other hand, the nature of the noncovalent Br-∗-Br interactions in Br_4–Br_{12} is classified by the *pure* CS interactions ($\theta \leq 76°$). The noncovalent Br-∗-Br interactions in the linear type clusters of Br_4 (C_s-L$_1$)–Br_{12} (C_s-L$_5$) are predicted to have the *p*-CS/*t*-HB$_{nc}$ nature ($90.6° \leq \theta_p$), except for r_2, outside the ones of the first end, which have the *p*-CS/vdW nature, although it is very close to the border area between the two ($\theta_p \leq 89.4°$). In the case of the cyclic clusters, the noncovalent Br-∗-Br interactions will have the *p*-CS/vdW nature ($\theta_p \leq 88.4°$), except for r_2 in Br_8 (S_4) ($\theta_p = 93.5°$) and Br_8 (S_4-Wm) ($\theta_p = 95.3°$), which have the *p*-CS/*t*-HB$_{nc}$ nature.

The energies for Br_3 σ(3c–4e) of the n_p(Br)$\rightarrow\sigma^*$(Br–Br) type are well evaluated by not only $E(2)$ but also C_{ii}^{-1} for Br_4 (C_s-L_1)–Br_{12} (C_s-L_5). $E(2)$ correlates very well to C_{ii}^{-1}. The CT interactions of the n_p(Br)$\rightarrow\sigma^*$(Br–Br) type must contribute to form Br_4 (C_s-L_1), which can be explained based on the MO energies, ε_i. However, it seems difficult to explain the stability of Br_4 (C_{2h}) and Br_4 (D_{2d}) based on the energies. The Br_2 molecules must be stacked more effectively in Br_4 (C_{2h}) and Br_4 (D_{2d}), resulting in shorter electronuclear distances on average. The energy lowering effect by $\Delta\Sigma_i{}^n H_c(i)$, due to the effective stacking of $2Br_2$ in Br_4 (C_{2h}) and Br_4 (D_{2d}), contributes to form the clusters, although the inverse contribution from $\Delta((\Sigma_{i\neq j}{}^n J_{ij} - \Sigma_{i\neq j,\|}{}^n K_{ij})/2)$ must also be considered.

Supplementary Materials: The following are available online, Table S1: Structural parameters for Br_2–Br_6, Table S2: Structural parameters for Br_8–Br_{12}, Table S3: The bond path distances and the straight-line distances in the polybromide clusters, together with the differences between the two, Table S4: The $\rho_b(r_c)$, $H_b(r_c) - V_b(r_c)/2$ ($=(\hbar^2/8m)\nabla^2\rho_b(r_c)$), and $H_b(r_c)$ values and QTAIM-DFA parameters for Br-∗-Br in polybromine clusters of Br_2–Br_{12}, Table S5: Contributions from the donor–acceptor (NBO(i)$\rightarrow$NBO(j)) interactions of the n(Br)$\rightarrow\sigma^*$(Br–Br) type in the optimized structures of Br_4–Br_{12}, calculated using NBO analysis, Table S6: MO energies of Br_4 (C_{2h}), Table S7: MO energies of Br_4 (D_{2d}), Table S8: MO energies of Br_2 ($D_{\infty h}$), Table S9: MO energies of Br_4 (C_s-L_1), Table S10: The $\Delta\varepsilon_i$ values for Br_4 (C_s-L_1), relative to $2Br_2$ ($D_{\infty h}$), Table S11: Energies for the Br_4 clusters and $2Br_2$, together with the differences between the two, Figure S1: Plot of ΔE_{ZP} versus ΔE_{ES} for Br_4–Br_{12}, relative to those of Br_2, respectively, Figure S2: Plots of ΔE_{ES} for Br_2–Br_{12} (C_s-L_n), Figure S3: Optimized structures for the cyclic bromine clusters of Br_8–Br_{12}, together with the linear type bromine cluster of Br_{10}, Figure S4: Plot of θ and θ_p versus R for the noncovalent Br-∗-Br interactions at the BCPs in the fully optimized structures of Br_4–Br_{12}, Figure S5: Plot of θ_p versus θ for the noncovalent Br-∗-Br interactions at the BCPs in the fully optimized structures of Br_4–Br_{12}, Figure S6: Plot of $E(2)$ versus R for noncovalent Br-∗-Br interactions in Br_4 (C_s-L_1)–Br_{12} (C_s-L_5), Figure S7: Plot of $E(2)$ versus θ for noncovalent Br-∗-Br interactions in Br_4 (C_s-L_1)–Br_{12} (C_s-L_5), Figure S8: Plot of $E(2)$ versus θ_p for noncovalent Br-∗-Br interactions in Br_4 (C_s-L_1)–Br_{12} (C_s-L_5), Figure S9: MO$_i$ ($i = 70$, 67, 64, 35, and 30) and the energies relative to those corresponding to $2Br_2$, and Cartesian coordinates and energies of all the species involved in the present work. Appendix: Survey of QTAIM, closely related to QTAIM dual-functional analysis; Criteria for classification of interactions: behavior of typical interactions elucidated by QTAIM-DFA; Characterization of interactions.

References and Notes

1. Colin, J.J. Sur Quelques Combinaisons de l'Iode. *Ann. Chim.* **1814**, *91*, 252–272.
2. Cavallo, G.; Metrangolo, P.; Pilati, T.; Resnati, G.; Terraneo, G. Halogen Bond: A Long Overlooked Interaction. In *Halogen Bonding I: Impact on Materials Chemistry and Life Sciences (Topics in Current Chemistry)*; Metrangolo, P., Resnati, G., Eds.; Springer: New York, NY, USA, 2015; Chapter 1; pp. 1–18.
3. Cavallo, G.; Metrangolo, P.; Milani, R.; Pilati, T.; Priimagi, A.; Resnati, G.; Terraneo, G. The Halogen Bond. *Chem. Rev.* **2016**, *116*, 2478–2601. [CrossRef]
4. Bent, H.A. Structural chemistry of donor-acceptor interactions. *Chem. Rev.* **1968**, *68*, 587–648. [CrossRef]

5.   Desiraju, G.R.; Parthasarathy, R. The nature of halogen halogen interactions: Are short halogen contacts due to specific attractive forces or due to close packing of nonspherical atoms? *J. Am. Chem. Soc.* **1989**, *111*, 8725–8726. [CrossRef]

6.   Metrangolo, P.; Resnati, G. Halogen Bonding: A Paradigm in Supramolecular Chemistry. *Chem. Eur. J.* **2001**, *7*, 2511–2519. [CrossRef]

7.   Erdélyi, M. Halogen bonding in solution. *Chem. Soc. Rev.* **2012**, *41*, 3547–3557. [CrossRef]

8.   Beale, T.M.; Chudzinski, M.G.; Sarwar, M.G.; Taylor, M.S. Halogen bonding in solution: Thermodynamics and applications. *Chem. Soc. Rev.* **2013**, *42*, 1667–1680. [CrossRef] [PubMed]

9.   Legon, A.C. Prereactive Complexes of Dihalogens XY with Lewis Bases B in the Gas Phase: A Systematic Case for the Halogen Analogue B⋯XY of the Hydrogen Bond B HX. *Angew. Chem. Int. Ed.* **1999**, *38*, 2686–2714. [CrossRef]

10. Politzer, P.; Murray, J.S.; Clark, T. Halogen bonding and other σ-hole interactions: A perspective. *Phys. Chem. Chem. Phys.* **2013**, *15*, 11178–11189. [CrossRef]

11. Sugibayashi, Y.; Hayashi, S.; Nakanishi, W. Behavior of Halogen Bonds of the Y–X⋯Type (X, Y=F, Cl, Br, I) in the Benzene p System, Elucidated by Using a Quantum Theory of Atoms in Molecules Dual-Functional Analysis. *Chem. Phys. Chem.* **2016**, *17*, 2579–2589. [CrossRef] [PubMed]

12. Desiraju, G.R.; Ho, P.S.; Kloo, L.; Legon, A.C.; Marquardt, R.; Metrangolo, P.; Politzer, P.; Resnati, G.; Rissanen, K. Definition of the halogen bond (IUPAC Recommendations 2013). *Pure Appl. Chem.* **2013**, *85*, 1711–1713. [CrossRef]

13. Metrangolo, P.; Resnati, G. (Eds.) *Halogen Bonding: Fundamentals and Applications*; Series Structure and Bonding; Springer: New York, NY, USA, 2008.

14. Gierszal, K.P.; Davis, J.G.; Hands, M.D.; Wilcox, D.S.; Slipchenko, L.V.; Ben-Amotz, D. π-Hydrogen Bonding in Liquid Water. *J. Phys. Chem. Lett.* **2011**, *2*, 2930–2933. [CrossRef]

15. *Categorizing Halogen Bonding and other Noncovalent Interactions Involving Halogen Atoms.* a satellite event of the XXII Congress and General Assembly of the International Union of Crystallography, 2010; https://doi.org/10.1515/ci.2010.32.2.20 (accessed on 1 May 2021).

16. Donohue, J.; Goodman, S.H. Interatomic distances in solid chlorine. *Acta Cryst.* **1965**, *18*, 568–569. [CrossRef]

17. Powell, B.M.; Heal, K.M.; Torrie, B.H. The temperature dependence of the crystal structures of the solid halogens, bromine and chlorine. *Mol. Phys.* **1984**, *53*, 929. [CrossRef]

18. Van Bolhuis, F.; Koster, P.B.; Migchelsen, T. Refinement of the crystal structure of iodine at 110° K. *Acta Cryst.* **1967**, *23*, 90–91. [CrossRef]

19. Schuster, P.; Mikosch, H.; Bauer, G. All electron density functional study of neutral and ionic polybromine clusters. *J. Chem. Phys.* **1998**, *109*, 1833–1844. [CrossRef]

20. Sung, D.; Park, N.; Park, W.; Hong, S. Formation of polybromine anions and concurrent heavy hole doping in carbon nanotubes. *Appl. Phys. Lett.* **2007**, *90*, 093502. [CrossRef]

21. Nakanishi, W.; Hayashi, S.; Narahara, K. Polar Coordinate Representation of $H_b(r_c)$ versus $(\hbar^2/8m)\nabla^2\rho_b(r_c)$ at BCP in AIM Analysis: Classification and Evaluation of Weak to Strong Interactions. *J. Phys. Chem. A* **2009**, *113*, 10050–10057. [CrossRef]

22. Nakanishi, W.; Hayashi, S. Atoms-in-Molecules Dual Functional Analysis of Weak to Strong Interactions. *Curr. Org. Chem.* **2010**, *14*, 181–197. [CrossRef]

23. Nakanishi, W.; Hayashi, S. Dynamic Behaviors of Interactions: Application of Normal Coordinates of Internal Vibrations to AIM Dual Functional Analysis. *J. Phys. Chem. A* **2010**, *114*, 7423–7430. [CrossRef]

24. Nakanishi, W.; Hayashi, S.; Matsuiwa, K.; Kitamoto, M. Applications of Normal Coordinates of Internal Vibrations to Generate Perturbed Structures: Dynamic Behavior of Weak to Strong Interactions Elucidated by Atoms-in-Molecules Dual Functional Analysis. *Bull. Chem. Soc. Jpn.* **2012**, *85*, 1293–1305. [CrossRef]

25. Nakanishi, W.; Hayashi, S. Role of dG/dw and dV/dw in AIM Analysis: An Approach to the Nature of Weak to Strong Interactions. *J. Phys. Chem. A* **2013**, *117*, 1795–1803. [CrossRef] [PubMed]

26. Bader, R.F.W. *Atoms in Molecules. A Quantum Theory*; Oxford University Press: Oxford, UK, 1990.

27. Matta, C.F.; Boyd, R.J. An Introduction to the Quantum Theory of Atoms in Molecules. In *The Quantum Theory of Atoms in Molecules: From Solid State to DNA and Drug Design*; WILEY-VCH: Weinheim, Germany, 2007.

28. Nakanishi, W.; Hayashi, S.; Nishide, T. Intrinsic dynamic and static nature of each HB in the multi-HBs between nucleobase pairs and its behavior, elucidated with QTAIM dual functional analysis and QC calculations. *RSC Adv.* **2020**, *10*, 24730–24742. [CrossRef]

29. See also Figure 5 for the definition of (R, θ) and (θ_p, κ_p), exemplified by the r_9 in Br_{10} (C_s-L_5).

30. Nakanishi, W.; Hayashi, S. Perturbed structures generated using coordinates derived from compliance constants in internal vibrations for QTAIM dual functional analysis: Intrinsic dynamic nature of interactions. *Int. J. Quantum Chem.* **2018**, *118*, e25590–e25591. [CrossRef]

31. The basic concept for the compliance constants was introduced by Taylor and Pitzer, followed by Konkoli and Cremer.

32. Taylor, W.T.; Pitzer, K.S. Vibrational frequencies of semirigid molecules: A general method and values for ethylbenzene. *J. Res. Natl. Bur. Stand.* **1947**, *38*, 1–17. [CrossRef]

33. Konkoli, Z.; Cremer, D. A new way of analyzing vibrational spectra. I. Derivation of adiabatic internal modes. *Int. J. Quantum Chem.* **1998**, *67*, 1–9. [CrossRef]

34. The C_{ij} are defined as the partial second derivatives of the potential energy due to an external force, as shown in Equations (R1), where *i* and *j* refer to internal coordinates, and the external force components acting on the system f_i and f_j correspond to *i* and *j*, respectively.

35. $C_{ij} = \partial^2 E / \partial f_i \partial f_j$ (R1).

36. The C_{ij} Values and the Coordinates Corresponding to C_{ii} Were Calculated by Using the Compliance 3.0.2 Program Released by Grunenberg, J. and Brandhorst, K. Available online: http://www.oc.tu-bs.de/Grunenberg/compliance.html (accessed on 1 May 2021).

37. Brandhorst, K.; Grunenberg, J. Efficient computation of compliance matrices in redundant internal coordinates from Cartesian Hessians for nonstationary points. *J. Chem. Phys.* **2010**, *132*, 184101. [CrossRef]

38. Brandhorst, K.; Grunenberg, J. How strong is it? The interpretation of force and compliance constants as bond strength descriptors. *Chem. Soc. Rev.* **2008**, *37*, 1558–1567. [CrossRef] [PubMed]

39. Grunenberg, J. III-defined concepts in chemistry: Rigid force constants vs. compliance constants as bond strength descriptors for the triple bond in diboryne. *Chem. Sci.* **2015**, *6*, 4086–4088. [CrossRef] [PubMed]

40. Frisch, M.J.; Trucks, G.W.; Schlegel, H.B.; Scuseria, G.E.; Robb, M.A.; Cheeseman, J.R.; Scalmani, G.; Barone, V.; Mennucci, B.; Petersson, G.A.; et al. *Gaussian 09 (Revision D.01)*, Gaussian, Inc.: Wallingford, CT, USA, 2009.

41. Binning, R.C.; Curtiss, L.A. Compact contracted basis sets for third-row atoms: Ga–Kr. *J. Comput. Chem.* **1990**, *11*, 1206–1216. [CrossRef]

42. Curtiss, L.A.; McGrath, M.P.; Blaudeau, J.-P.; Davis, N.E.; Binning, R.C., Jr.; Radom, L. Extension of Gaussian-2 theory to molecules containing third-row atoms Ga–Kr. *J. Chem. Phys.* **1995**, *103*, 6104–6113. [CrossRef]

43. McGrath, M.P.; Radom, L. Extension of Gaussian-1 (G1) theory to bromine-containing molecules. *J. Chem. Phys.* **1991**, *94*, 511–516. [CrossRef]

44. Clark, T.; Chandrasekhar, J.; Spitznagel, G.W.; Schleyer, P.v.R. Efficient diffuse function-augmented basis sets for anion calculations. III. The 3-21+G basis set for first-row elements, Li–F. *J. Comput. Chem.* **1983**, *4*, 294–301. [CrossRef]

45. Møller, C.; Plesset, M.S. Note on an Approximation Treatment for Many-Electron Systems. *Phys. Rev.* **1934**, *46*, 618–622. [CrossRef]

46. Gauss, J. Effects of electron correlation in the calculation of nuclear magnetic resonance chemical shifts. *J. Chem. Phys.* **1993**, *99*, 3629–3643. [CrossRef]

47. Gauss, J. Accurate Calculation of NMR Chemical Shifts. *Ber. Bunsen-Ges. Phys. Chem.* **1995**, *99*, 1001–1008. [CrossRef]

48. Biegler-König, F.; Schönbohm, J. The AIM2000 Program (Version 2.0). Available online: http://www.aim2000.de (accessed on 1 May 2021).

49. Biegler-König, F. Calculation of atomic integration data. *J. Comput. Chem.* **2000**, *21*, 1040–1048. [CrossRef]

50. Keith, T.A. AIMAll (Version 17.11.14), TK Gristmill Software, Overland Park KS, USA. 2017. Available online: http://aim.tkgristmill.com (accessed on 1 May 2021).

51. See Figure 3 for Br$_4$–Br$_{12}$ of the L-shaped clusters in the C_s symmetry, Br$_4$ (C_s-L$_1$)–Br$_{12}$ (C_s-L$_5$), and Figure 4 for Br$_6$–Br$_{12}$ of the cyclic bromine clusters.

52. See also Entry 1 in Table 3. http://aim.tkgristmill.com/ (accessed on 1 May 2021).

53. The Br–Br distance in Br$_2$ was optimized to be 2.2806 Å with MP2/6-311+G(3df), which was very close to the observed distance in the gas phase (2.287 Å). However, the values are shorter than that determined by the X-ray crystallographic analysis (2.491 Å) by 0.210 Å. The non-covalent Br—Br distance is 3.251 Å in crystal, which is shorter than the sum of the van der Waals radii by 0.45 Å.

54. Bondi, A. van der Waals Volumes and Radii. *J. Phys. Chem.* **1964**, *68*, 441–451. [CrossRef]

55. The molecular graph for Br$_4$ (C_{2h}) was very complex and very different from that expected for it when calculated with MP2/6-311+G(3df)//MP2/6-311+G(3df). Some (ω,σ) = (3, −3) attractors appear in the molecular graph of Br$_4$ (C_{2h}), which do not correspond to bromine atoms. Therefore, the molecular graph for Br$_4$ (C_{2h}) were drawn with MP2/6-311+G(d)//MP2/6-311+G(3df), which was shown in Figure 2. The $\rho_b(r_c)$, $H_b(r_c) - V_b(r_c)/2$ ($=(\hbar^2/8m)\nabla^2\rho_b(r_c)$), and $H_b(r_c)$ values were calculated with the same method.

56. Glendening, E.D.; Reed, A.E.; Carpenter, J.E.; Weinhold, F. *NBO*, Gaussian, Inc.: Pittsburgh, PA, USA, 2003; version 3.1.